EVALUATION OF RADIATIVE HEAT TRANSFER FOR INTERPLANETARY RE-ENTRY UNDER VIBRATIONAL NONEQUILIBRIUM CONDITIONS

C. M. Mazzoni[(1)], D. Lentini[(1,*)], G. D'Ammando[(2)], R. Votta[(3)]

[(1)]Dip. Ingegneria Meccanica e Aerospaziale, Sapienza Università di Roma, Via Eudossiana 18, I-00184 Roma

[(2)] Dip. Chimica, Università degli Studi di Bari, Via Orabona 4, I-70125 Bari

[(3)]Aerothermodynamics and Combustion Research Laboratory, CIRA, Via Maiorise, I-81083 Capua

[(*)]Corresponding author, diego.lentini@uniroma1.it

ABSTRACT

A radiative heat transfer code, based on the Discrete Transfer method, is use in combination with a spectral radiative database and a thermochemical nonequilibrium Navier-Stokes flowfield solver, to compute radiative heating under vibrational nonequilibrium conditions for the re-entry test vehicle FIRE II. The trajectory point under scrutiny refers to a flight velocity of 8.3 km/s, where radiative equilibrium prevails. Numerical predictions indicate a quite good agreement with experimental data, both for the radiative intensity along the stagnation streamline and for the total (convective plus absorbed radiative) heat flux at the stagnation point. The Discrete Transfer method makes the code applicable to arbitrarily complex geometries, and the vibrational nonequilibrium description allows considering re-entry from Lunar or interplanetary return trajectories, as well as from terrestrial orbits.

NOMENCLATURE

I number of θ intervals

I_λ spectral radiative intensity

J number of ψ intervals

j_λ^e spectral emissivity coefficient

k_λ spectral absorption coefficient

L_{ij} number of integration intervals along lines-of-sight identified by indices i and j

$\hat{n}$ inward-pointing unit vector

$q_\lambda{}^r$ spectral radiative heat flux

s abscissa along line-of-sight

$\hat{s}$ unit vector identifying direction of line-of-sight

T temperature

x Cartesian coordinate

α wall absorptance

φ_{ij} angle between $\hat{n}$ and $\hat{s}$

λ wavelength

Λ number of spectral intervals

ψ azimuth

θ latitude

Ω solid angle

Subscripts

e electronic

r rotational

tot total

vib vibrational

W wall

λ wavelength

∞ ambient

Superscripts

c convective

r radiative

1. INTRODUCTION

Many space missions envision the use of aerobraking re-entry techniques to return payloads from geostationary, lunar or interplanetary orbits. Aerobraking takes advantage of aerodynamic drag to reduce the momentum of the re-entry body. The design of such vehicles requires knowledge of the

total heating environment. Because of the high altitudes and speeds involved, especially in the case of re-entry from lunar or interplanetary orbits, the temperature behind the bow shock preceding the blunt-nosed body can attain tens of thousand degrees Kelvin. In such conditions, thermal radiation makes a significant contribution to the overall heat load on the body, and accordingly needs to be correctly modelled when designing heat shields. The exceptionally high temperature levels, together with the low pressure prevailing at high altitude, imply that significant vibrational nonequilibrium effects are anticipated; therefore, the tools used to predict the heating environment must account for nonequilibrium [1].

The importance of comparing results from computational simulations to the ones from flight experiments cannot be overemphasized. Among the several experiments flown up to the present, one of the most detailed is certainly FIRE II, carried out in the 60's. The FIRE project was designed to provide data on the aerothermal environment surrounding a blunt body during interplanetary reentry into the Earthfs atmosphere at a nominal velocity of 11.35 km/s. It provides a great wealth of data [2, 3], taken at various points along the re-entry trajectory, spanning flow regimes from highaltitude, high-velocity, largely nonequilibrium flows to relatively low-altitude, low-velocity, equilibrium flows. The test case analysed in the present paper is the 1648 s FIRE II trajectory point. The FIRE II experiments have been the subject of several computational studies, including those by Greendyke and Hartung [4], Olynick et al. [5], Johnston et al. [6]. The first two papers use a thermochemical nonequilibrium Navier-Stokes solver, while the third is based on a viscous shock layer method [7]. As far as spectral radiation modeling is concerned, they adopt similar approaches, namely the smeared rotational band (SRB) model developed by Patch et al. [8] and first applied to entry problems by Hartung [9]. The populations of electronically excited states governing radiation are calculated assuming either a Boltzmann distribution [5] or a non-equilibrium distribution using the quasi-steady-state (QSS) method [4,6]. Papers [4-6] are taken as the reference works for the investigation reported in the present paper. A feature common to [4-6] is that they use the tangent slab approximation to calculate the radiative heat flux and its divergence (the latter being the quantity coupling the flowfield to the radiation field). Such a treatment amounts to considering the contribution of radiation only in the direction normal to the surface of the body, which may be a roughly acceptable approximation for a blunt-nosed body, but is certainly inapplicable to complex geometries, e.g., winged bodies. In order to overcome this limitation, in the present paper a much more powerful solver for the Radiative Transfer Equation (RTE) is adopted, based on the Discrete Transfer method [10], which allows handling arbitrary geometries with a prescribed accuracy.

The aim of the present study is to examine the FIRE II heat transfer data and to compare them to numerical results computed on the basis of a CFD solution worked out at CIRA (Centro Italiano

Ricerche Aerospaziali) by means of CAST, a nonequilibrium Navier-Stokes CFD code developed under the aegis of ASI (Agenzia Spaziale Italiana). CAST [11] is a Reynolds-Averaged Navier Stokes CFD code that solves the RANS equations on structured multi-block grids using a finite volume second-order upwind scheme (FDS or AUSM) for spatial discretization, and explicit or implicit schemes for time integration. Viscous fluxes are computed with a classical centered scheme. It can use both 5 and 11 species air as operating fluid with chemical kinetics and transport properties taken from the literature [12-15] or in-house models [16]. Turbulence effects are described by different models such as Spalart-Allmaras, the two-equation standard k-ε (also with the inclusion of compressibility effects, the option chosen in the present work) and the RNG k-ε [17]. In the present work, thermal radiation is evaluated by post-processing the CFD solution via a code developed at the Dipartimento di Ingegneria Meccanica e Aerospaziale, Sapienza Universita di Roma, termed XENIOS-RADIATION (derived from the in-house CFD code XENIOS [18]), adopting the Discrete Transfer method, which integrates the RTE along a finite number of rays, or lines-of-sight. This method allows controlling the accuracy of the resulting solution, and the ensuing CPU cost, by prescribing the number of lines-of-sight, as well as the integration step size along them. Coupling between thermal radiation and CFD solution is obtained by iteratively feeding the computed term of the divergence of the radiative heat flux, as determined by XENIOS-RADIATION, back to the energy equation solver in the CAST code. XENIOS-RADIATION, inter alia, includes account for the vibrational temperatures of the component species. The emissivity and absorption coefficient of high-temperature air are described by a multi-group spectral model [19], partitioning the spectral range of interest into a discrete number of intervals, with wavelength larger than the characteristic width of atomic and diatomic rotational lines, and calculating both an average emissivity and an average absorption coefficient over each interval. The multi-group spectral database, generated by a code termed Mspec developed at the Dipartimento di Chimica, Università degli Studi di Bari, is parametrized by a limited number of internal temperatures, in addition to the individual species number densities, thereby making allowance for nonequilibrium in the multi-temperature approach.

2. SPECTRAL DATABASE

The analysis of radiative heat transfer for entry of space vehicles into the atmosphere requires suitable models to describe the absorption k_λ and emissivity j_λ^e of the high temperature plasma created by the hypersonic shock. In this work the spectral properties of high temperature air are described by a simple band model, partitioning the spectral range into intervals, and using pre-computed tables of average values of k_λ and j_λ^e over each interval.

High-resolution spectral coefficients have been calculated using the code PARADE [20], taking into account atomic and molecular bound-bound, atomic bound-free and electron-ion free-free radiative processes. The following species are considered: N, O, N^+, O^+, N_2, O_2, NO, N_2^+, O_2^+, NO^+, e^-. The molecular bound-bound emissive systems included in the database are reported in Tab. 1. The molecular spectroscopic data necessary for the calculation of O_2^+ and NO^+ high-resolution spectra have been provided by prof. S.T. Surzhikov [21], since they were not present in the version of PARADE used to generate the tables.

The initial single species high-resolution spectra, calculated at a reference total pressure of 1 atm and an electron number density of 1022 m^{-3} over the spectral range 0.01-5 μm, have been averaged over 2500 uniformly spaced wavelength intervals and tabulated as a function of temperature. For atomic radiation and the free-free continuum, the tables report the average absorption coefficient and emissivity of each group as a function of the electronic temperature T_e. In the case of diatomic molecules, the group coefficients have been tabulated as a function of two independent temperatures, the vibrational temperature T_v and the rotational temperature T_r. The temperature ranges and the number of independent variables chosen to tabulate the average spectral coefficients of each radiative process are reported in Tab. 2. These tabulations are the input data to the Mspec code that performs a further pre-processing, removing groups external to the investigated range and averaging a number of adjacent groups, depending on the spectral range and number of intervals selected in a specific radiative transfer calculation.

Finally, the total mixture coefficients at each point in the flow are calculated by combining the pre-processed single species group coefficients according to the species number densities and corresponding temperatures in each grid cell. While the method works well for the broadband molecular radiation, it may produce inaccurate results for the bound-bound atomic radiation, characterized by relatively few lines with strongly varying intensities, and widths distributed over large spectral ranges. This problem may be partly overcome by increasing the number of bands used in the simulation. The method is expected to provide adequate accuracy for radiation transfer calculation, and its main advantages are the much reduced memory requirements with respect to a detailed line-by-line spectral calculation and the avoidance of line shape functions, which is generally the most time-consuming part in a line-by-line code.

3. NONEQUILIBRIUM RADIATION SOLUTION MODEL

The Radiative Transfer Equation is evaluated by means of the Discrete Transfer method [10]. It amounts to a directional ordinary differential equation, which for participating, non-scattering media takes on the form, along the generic direction defined by unit vector $\hat{s}$

$$\frac{dI_\lambda}{ds} = \hat{s} \cdot \nabla I_\lambda = j_\lambda^e - k_\lambda I_\lambda \tag{1}$$

By assuming a directional coordinate along $\hat{s}$, with origin at the boundary of the domain, the formal solution of the RTE at the directional ascissa s, corresponding to the Cartesian coordinates $\vec{x}$, is:

$$I_\lambda(\vec{x},\hat{s}) = I_\lambda(s,\hat{s}) = I_\lambda(0,\hat{s}) \exp\left(-\int_0^s k_\lambda(s',\hat{s})ds'\right) + \int_0^s j_\lambda^e(s',\hat{s}) \exp\left(-\int_{s'}^s k_\lambda(s'',\hat{s})ds''\right)ds' \tag{2}$$

where $I_\lambda(0,\hat{s})$ is the value of the spectral radiative intensity at the boundary.

The spectral values of the radiative heat flux and of its divergence at point $\vec{x}$, can then be expressed as

$$q_\lambda^r(\vec{x}) = \vec{q}_\lambda^r \cdot \hat{n} = \int_{2\pi} I_\lambda(\vec{x},\hat{s})\hat{n} \cdot \hat{s} d\Omega \tag{3}$$

$$\nabla \cdot \vec{q}_\lambda^r(\vec{x}) = 4\pi j_\lambda^e(\vec{x}) - k_\lambda(\vec{x}) \int_{4\pi} I_\lambda(\vec{x},\hat{s}) d\Omega \tag{4}$$

with $\hat{n}$ denoting the inward-pointing unit vector normal to the referenced surface and $d\Omega$ representing the incremental solid angle along direction $\hat{s}$.

The Discrete Transfer method solves Eqs. (2)-(4) by a double discretization process, one over the overall solid angle, in order to extract a finite number of directions along which the RTE is solved, and the other along each such directions, to integrate the RTE. Equation (1) is solved at any of Cartesian coordinates $\vec{x}$ along a finite discrete number of lines-of-sight. Such directions are defined in the Cartesian frame by a latitude θ and an azimuth ψ, by dividing the whole solid angle of 4π steradians, as seen by the point under scrutiny, into incremental solid angles along these directions; the range of θ (from $-\pi$ to $+\pi$) is dividided into I values, and similarly the range of ψ (from 0 to 2π) into J values. A directional coordinate s is defined along each line-of-sight, with the origin at the point $\vec{x}$ under scrutiny; the length of the line-of-sight in direction i-j is subdivided into L_{ij} intervals (with running indices l and m). In this way, the integral along any direction can be evaluated as a summation, e.g., Eq. (2) can be expressed in discretized form as

$$I_{\lambda ij}(\vec{x}) = I_{\lambda \infty ij} \exp\left(-\sum_{l=1}^{L_{ij}} k_{\lambda l} \Delta s_l\right) + \sum_{m=1}^{L_{ij}} j_{\lambda m}^e \exp\left(-\sum_{l=1}^{m} k_{\lambda l} \Delta s_l\right) \Delta s_m \tag{5}$$

where $I_{\lambda_\infty ij}$ denotes the spectral radiative intensity at the far away extreme of line-of-sight *i-j* (e.g., at a solid boundary), k_{λ_l} and $j^e_{\lambda_l}$ stand for the spectral values of the absorption and emission coefficients at ascissa s_l along the line-of-sight, and Δs_l represents the size of the *l*-th integration step.

Note that the Cartesian coordinates of the point at abscissa s_l along the line-of-sight in direction *i-j* can be expressed, if ψ is assumed to lie in the x-y plane, as

$$\begin{aligned} x_l &= x + s_l \cos\theta_i \cos\psi_j \\ y_l &= y + s_l \cos\theta_i \sin\psi_j \\ z_l &= z + s_l \sin\theta_i \end{aligned} \tag{6}$$

In the Discrete Transfer method, the integral over the whole solid angle can be evaluated as a summation over a finite number of directions. Accordingly, the resulting discretized expressions for the *spectral* radiative heat flux and its divergence at point $\vec{x}$ are

$$\vec{q}^{\,r}_\lambda(\vec{x}) = \sum_{i=1}^{I}\sum_{j=1}^{J} I_{\lambda_{ij}}(\vec{x})\cos\varphi_{ij}\Delta\Omega_{ij} \tag{7}$$

$$\nabla\cdot\vec{q}^{\,r}_\lambda(\vec{x}) = 4\pi j^e_\lambda(\vec{x}) - k_\lambda(\vec{x})\sum_{i=1}^{I}\sum_{j=1}^{J} I_{\lambda_{ij}}(\vec{x})\Delta\Omega_{ij} \tag{8}$$

where φ_{ij} is the angle between $\hat{n}$ and $\hat{s}$, and $\Delta\Omega_{ij}$ is the incremental solid angle defined as

$$\Delta\Omega_{ij} = \cos\theta_i \Delta\theta_i \Delta\psi_j \tag{9}$$

The *integral* values of radiative intensity, radiative heat flux and its divergence can be computed from the spectral ones, see Eqs. (2)-(4), simply by means of an integration over the total wavelength range:

$$\begin{aligned} I(\vec{x},\hat{s}) &= \int_0^\infty I_\lambda(\vec{x},\hat{s})d\lambda \\ q^r(\vec{x}) &= \int_0^\infty q^r_\lambda(\vec{x})d\lambda \\ \nabla\cdot q^r(\vec{x}) &= \int_0^\infty \nabla\cdot q^r_\lambda(\vec{x})d\lambda \end{aligned} \tag{10}$$

Unlike other models, the Discrete Transfer method converges to the exact solution; further, it also

allows controlling the accuracy of the resulting solution and, obviously, the computational costs in term of CPU time and required memory, by prescribing the number of lines-of-sight and the integration step size along them. Its most complex and problematic facet is the tracing of the rays, and their interaction with the computational domain; dedicated algorithms are required to manage these crucial issues. Such topics are overcome in XENIOS-RADIATION by an original ray-tracing algorithm, based on the Finite Element Method (FEM) [18]. Along each line-of-sight, the RTE integration step is allowed to vary, by taking it proportional to the characteristic length of the domain element being traversed; this option allows attaining a good compromise between intended level of accuracy and computational cost, while also minimizing errors due to the FEM intrinsic approximations. At any rate, the FEM approach allows the code to handle very complex geometries. The use of the multi-group model to describe high-temperature air radiative properties introduces a further degree of discretization, partitioning the spectral range of interest into a given number Λ of intervals of wavelengths $\Delta\lambda_i$, and calculating average values of the emissivity and absorption terms over each interval. The integral over the wavelength range can be evaluated as a summation over the number of spectral intervals. The resulting *integral* quantities, after Eq. (10), can be recovered as

$$\begin{aligned} I(\vec{x},\hat{s}) &= \sum_{\lambda=1}^{\Lambda} I_\lambda(\vec{x},\hat{s})\Delta\lambda_\lambda \\ q^r(\vec{x}) &= \sum_{\lambda=1}^{\Lambda} q^r_\lambda(\vec{x})\Delta\lambda_\lambda \\ \nabla\cdot q^r(\vec{x}) &= \sum_{\lambda=1}^{\Lambda} \nabla\cdot q^r_\lambda(\vec{x})\Delta\lambda_\lambda \end{aligned} \tag{11}$$

The number of wavelength intervals accordingly represents an additional degree of control, with implications on the accuracy of the solution and on the resulting computational cost. However, the width of each wavelengths interval must be larger than the characteristic one of diatomic and rotational lines.

4. RESULTS

XENIOS-RADIATION can compute radiative heat transfer either uncoupled or coupled (by using the formulation [22]) to the CFD solution by code CAST. Results shown here refer to the FIRE II trajectory point at 1648 s, see Tab. 3. At this point, the flow velocity is relatively low (8.30 km/s), ionization begins to fall off and the flow regime lies close to radiative equilibrium (i.e., radiative heat transfer does not significantly affect the flowfield, as also indicated in [5]). As a consequence, the coupling between the thermal radiation field and the CFD turns out to be relatively weak, and accordingly XENIOS-RADIATION is used here in an uncoupled fashion. Further, a 5-species

atmosphere model suffices to describe high-temperature air around the FIRE II capsule (N, O, NO, O_2, N_2).

The 3-D solution grid used in the present simulations, shown in Fig. 1, features 80540 cell elements. The current (i.e., at the given time, since ablation continuously removes material) FIRE II forebody shape is used for the heat shields [3]. The grid for the solution of the RTE features instead 100 rays per node, a value which has been found to ensure grid-independent results.

The flowfield, as determined by CAST, shows peak temperatures about eleven thousands degrees Kelvin reached in the shock-layer zone, see Figs. 2 and 3.

Note that, in the present investigation, the spectral region considered to evaluate radiation is between 0.05-4 μm. This range is partitioned in 100 intervals in the multi-group description. However, XENIOS-RADIATION results indicate that thermal radiation above 1.5 μm can reasonably be disregarded, in agreement with [4]. The spectral radiative intensity at the stagnation point along the stagnation streamline, and the spectral radiative heat flux at the stagnation point are plotted in Figs. 4 and 5, respectively; the negligible contribution of wavelengths above 1.5 μm can be appreciated.

The near-equilibrium nature of the flow, due to the relatively low-altitude and high-density conditions prevailing, can be inferred by the almost linear profile of the integral radiative intensity in the direction of the stagnation streamline, as shown in Fig. 6, with each gas layer contributing an equal increment to the total intensity at the wall, because of the smooth temperature profile (see Fig. 3). The profile of the radiative heat flux shown in Fig. 7 instead, after an initial linear trend, shows a second peak in the shock-layer zone, probably produced by 3-D radiative effects.

Fig. 8 shows the field of the divergence of the radiative heat flux, as computed by XENIOS-RADIATION. In line with its definition as the difference between emitted and absorbed radiative energy per unit time and volume [23], the divergence assumes high positive values in the zone behind the shock ahead of the body, where temperature levels and radiative emission are highest, as also indicated in Fig. 9.

The comparison between numerical heat transfer results and flight data from the FIRE II experiment focuses on two key quantities. The first is the radiative intensity above a wavelength of 0.2 μm along the stagnation streamline, measured by a near-stagnation point radiometer with a quartz window. The second is the total heat flux at the stagnation point, i.e., the convective heat flux plus the fraction of the radiative flux absorbed by the wall ($q_{tot}=q^c+\alpha q^r$), measured by a total calorimeter in the heat shield, at a location just off the stagnation point. The spectral profile of the surface absorptance of the beryllium heat shields is obtained from [3].

The experimental data used for comparison in this study are listed in Tab. 4, as taken from [4],

interpreted and/or extrapolated from the graphs in [2] and [3]. A further comparison is carried out with numerical results by [4-6], which adopt instead a different RTE solver method, envisaging merely a *single* direction (normal to the wall) for its integration, but a more accurate spectral description; such numerical results are listed in Tab. 4 below.

Predictions by XENIOS-RADIATION in terms of radiative intensity at the stagnation point along the stagnation streamline (above 0.2 μm), and wall radiative heat flux at the stagnation point are shown in Figs. 6 and 7, respectively. Incident and absorbed wall radiative heat flux fields are plotted in Figs. 10 and 11, respectively.

A comparison with both experimental data and numerical predictions by other authors is given in Tab. 4, reporting key quantities, i.e., the integral (in the range 0.2 to 4 mm) radiative intensity, the total heat flux at the wall, and the radiative flux absorbed by beryllium (for which, unfortunately, no measurement is available). Comparison with other authors' results require some comment. In particular, Ref. [5] reports both uncoupled and coupled solutions, which however turn out to be extremely close, thereby demonstrating the near-equilibrium condition prevailing at the time (1648 s) under consideration; the two different solutions are therefore assimilated to a single value within a two-digit accuracy. Notice anyway that [5] assumes the wall to radiate as a black body. Also Ref. [6] computes both uncoupled and coupled solutions, again very close to one another. Further, it reports predictions assuming both non-catalytic wall (as considered in Tab. 4) and semi-catalytic wall, the latter featuring a higher discrepancy with respect to experimental data (e.g., the total heat flux attains 7.85 MW/m^2), and are accordingly discarded here. On the whole, the present results emphasize a major improvement with respect to predictions of Refs. [4-6] with the only exception of the total heat flux, for which model [6] indicated a better agreement. On the other hand, the predictions of radiative intensity in Ref. [6] are in much worse agreement with experimental results than the ones by the present model.

5. CONCLUDING REMARKS

Predictions by XENIOS-RADIATION indicate a quite good agreement for the re-entry trajectory point at 1648 s which, as already mentioned, exhibits conditions close to radiative equilibrium.

In spite of a less accurate spectral treatment with respect to [4-6], XENIOS-RADIATION yields better estimates of radiative heat transfer, thanks to the inherently higher accuracy of the RTE solver, based on the Discrete Transfer method. This method allows, *inter alia*, handling arbitrarily complex geometries.

Further, the relatively low-temperature conditions of the case under scrutiny allow to disregard the coupling between CFD solution and thermal radiation. Coupling between CFD and radiation occurs

via the divergence of the radiative heat flux term, appearing in the energy equation. It turns out to be essential for really high-temperature and radiative nonequilibrium flows. At any rate, in the present implementation, coupling can be achieved via an iterative strategy: the flowfield is initially converged without the radiation term; once the initial solution is obtained, radiation is turned on and convergence continues with periodic updates of the radiative field.

Future work will involve testing the XENIOS-RADIATION code in conditions where coupling is essential, e.g., really high-velocity, high-temperature, strongly radiative nonequilibrium flows. Moreover, the spectral model will be improved with random models of atomic lines [24] for a more accurate calculation of atomic radiation within the framework of the multi-group approach.

ACKNOWLDEGMENTS

The authors are pleased to acknowledge helpful suggestions by G. Colonna (Istituto di Chimica del Plasma, CNR), A. Schettino (CIRA) and Prof. F. Nasuti (Sapienza Universita di Roma). Prof. S.T. Surzhikov (Institute of Problems of Mechanics, Russian Academy of Sciences) provided data for O_2^+ and NO^+. Research supported by grant ASI.

REFERENCES

[1] Park, Nonequilibrium Hypersonic Aerothermodynamics, Wiley, New York, 1990.

[2] E. S. Cornette, Forebody Temperatures and Calorimeter Heating Rates Measured During Project FIRE II Reentry at 11.35 Kilometers per Second, NASA TM X-1305, 1966.

[3] D. L. Cauhon, Radiative Heating Results from the FIRE II Flight Experiment at a Reentry Velocity of 11.4 Kilometers per Second, NASA TM X-1402, 1967.

[4] R. B. Greendyke and L. C. Hartung, Predicting Convective and Radiative Heat Transfer Analysis for the FIRE II Forebody, *J. Spacecraft and Rockets*, vol. 31, pp. 986-992, 1994.

[5] D. R. Olynick, W.D. Henline, L. H. Chambers and G. V. Chandler, Comparison of Coupled Radiative Navier-Stokes Flow Solutions with the Project FIRE II Flight Data, AIAA-94-1955, 1994.

[6] C. O. Johnston, B. R. Hollis and K. Sutton, Nonequilibrium Stagnation-Line Radiative Heating for Fire II, *J. Spacecraft and Rockets*, vol. 45, pp. 1185-1195, 2008.

[7] R. T. Davis, Numerical Solution of the Hypersonic Viscous Shock-Layer Equations, *AIAA J.*, vol. 8, pp. 843-851, 1970.

[8] R. W. Patch, W. L. Shackleford and S. S. Penner, Approximate Spectral Absorption Coefficient Calculation for Electronic Band Systems Belonging to Diatomic Molecules, *J. Quantitative Spectroscopy and Radiative Transfer*, vol. 2, pp. 263-271, 1962.

[9] L. C. Hartung, Predicting Radiative Heat Transfer in Thermochemical Nonequilibrium Flow Fields, NASA TM 4564, 1994.

[10] F. C. Lockwood and N. G. Shah, A New Radiation Solution Method for Incorporation in General Combustion Prediction Procedures, 18th Symp. (Int.) on Combust., The Combustion Institute, Pittsburgh, pp. 1405-1414, 1981.

[11] L. Cutrone, A. Mastellone, G. Ranuzzi, A. Schettino and A. Matrone, CIRA/CAST/DT-78 Software Design CAST V.1, 2011.

[12] C. Park, A Review of Reaction Rates in High Temperature Air, AIAA- 89-1740, 1989.

[13] R. C. Millikan and D. R. White, Systematics of Vibrational Relaxation, *J. Chem. Phys*., vol. 39, pp. 3209-3213, 1963.

[14] C. Park C. and S. H. Lee, Validation of Multi-Temperature Nozzle Flow Code NOZNT, AIAA-93-2862, 1993.

[15] K. S. Yun and E. A. Mason, Collision Integrals for the Transport Properties of Dissociating Air at High Temperatures, *Phys. Fluids*, vol. 39, pp. 3209-3213, 1962.

[16] M. Capitelli, G. Colonna, F. Esposito, I. Armenise, D. Pietanza and A. Laricchiuta, DT-2: Nota tecnica sui modelli per la termochimica: modelli macroscopici in dissociazione/ricombinazione, UNIBA/CAST/DT-2/REV. 4, 2009.

[17] F. Grasso and D. Falconi, High-Speed Turbulence Modeling of Shock-Wave/Boundary-Layer Interaction, *AIAA J.*, vol. 31, pp. 1199-1206, 1993.

[18] P. Venturini, D. Borello, C. Iossa, D. Lentini and F. Rispoli, Modeling of Multiphase Combustion and Deposit Formation in a Biomass-fed Furnace, *Energy*, vol. 35, pp. 3008-3021, 2010.

[19] S. T. Surzhikov, Radiation Modeling in Shock-Tubes and Entry Flows, AVT-162 RTO AVT/VKI Lecture Series, von Karman Institute, 2009.

[20] A. J. Smith, A. Wood, J. Dubois, M. Fertig, B. Pfeiffer and L. Marraffa, Plasma Radiation Database PARADE v2.2, TR28/96 issue 3, 2006.

[21] S. T. Surzhikov, private communication, 2010.

[22] B. Marracino and D. Lentini, Radiation Modelling in Non-Luminous Nonpremixed Turbulent Flames, *Combust. Sci. Tech.*, vol. 128, pp. 23-48, 1997.

[23] M. F. Modest, Radiative Heat Transfer, 2nd Ed., Academic Press, San Diego, 2003.

[24] S. Surzhikov, Random Models of Atomic Lines for Calculation of Radiation Transfer in Laser Supported Combustion and Shock Waves, AIAA-97-2367, 1997.

LIST OF TABLE CAPTIONS

Table 1

Molecule	Electronic systems
N_2	$B^3\Pi_g - A^3\Sigma_u^+$ $C^3\Pi_u - B^3\Pi_g$ $b^1\Sigma_u^+ - X^1\Sigma_g^+$
N_2^+	$B^2\Sigma_u^+ - X^3\Sigma_g^+$ $A^2\Pi_u - X^2\Sigma_g^+$
NO	$B^2\Pi - X^2\Pi$ $A^2\Sigma^+ - X^2\Pi$ $C^2\Pi - X^2\Pi$ $D^2\Sigma - X^2\Pi$
NO^+	$A^1\Pi - X^1\Sigma^+$
O_2	$B^3\Sigma_u^- - X^3\Sigma_g^-$
O_2^+	$A^2\Pi_u - X^2\Pi_g$ $b^4\Sigma_g^- - a^4\Pi_u$

Table 2

Process	**Function of**	***T* range [K]**
Atomic bound-bound	T_e	2000-60000
Molecular bound-bound	$T_e(=T_{vib})$, T_r	2000-40000
Atomic bound-free	T_e	2000-60000
Electron-ion free-free	T_e	2000-60000

Table 3

Altitude [km]	**Velocity [km/s]**	**Density [kg/m^3]**	T_∞ **[K]**	T_W **[K]**
42.14	8.30	$3.00 \cdot 10^{-3}$	267	1560

Table 4

Data	***I* (0.2-4.0 µm) [kW/(m^2 sr)]**	**q_{tot} [MW/m^2]**	**αq^r [MW/m^2]**
Experimental [2, 3, 4]	50	7.3	n.a.
Numerical [4] (error)	70 (+40%)	62 (-14.9%)	0.4
Numerical [5] (error)	80 (+60%)	8 (+9.6%)	0.52
Numerical [6] (error)	72.2 (+44.4%)	7.18 (-1.7%)	0.25
Numerical, present approach (error)	41.1 (-17.8%)	6.72 (-8%)	1.28

LIST OF FIGURE CAPTIONS

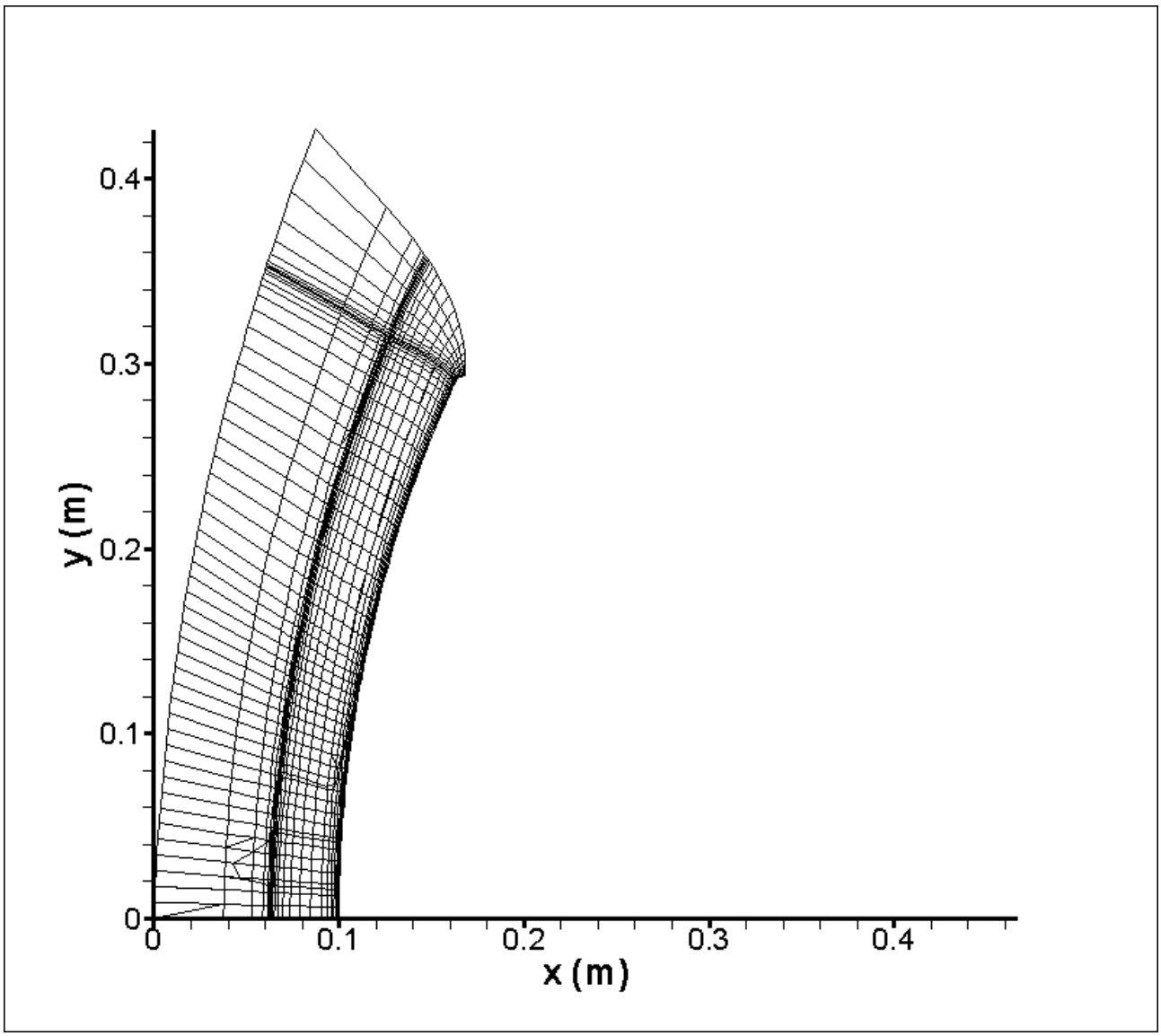

Figure 1.

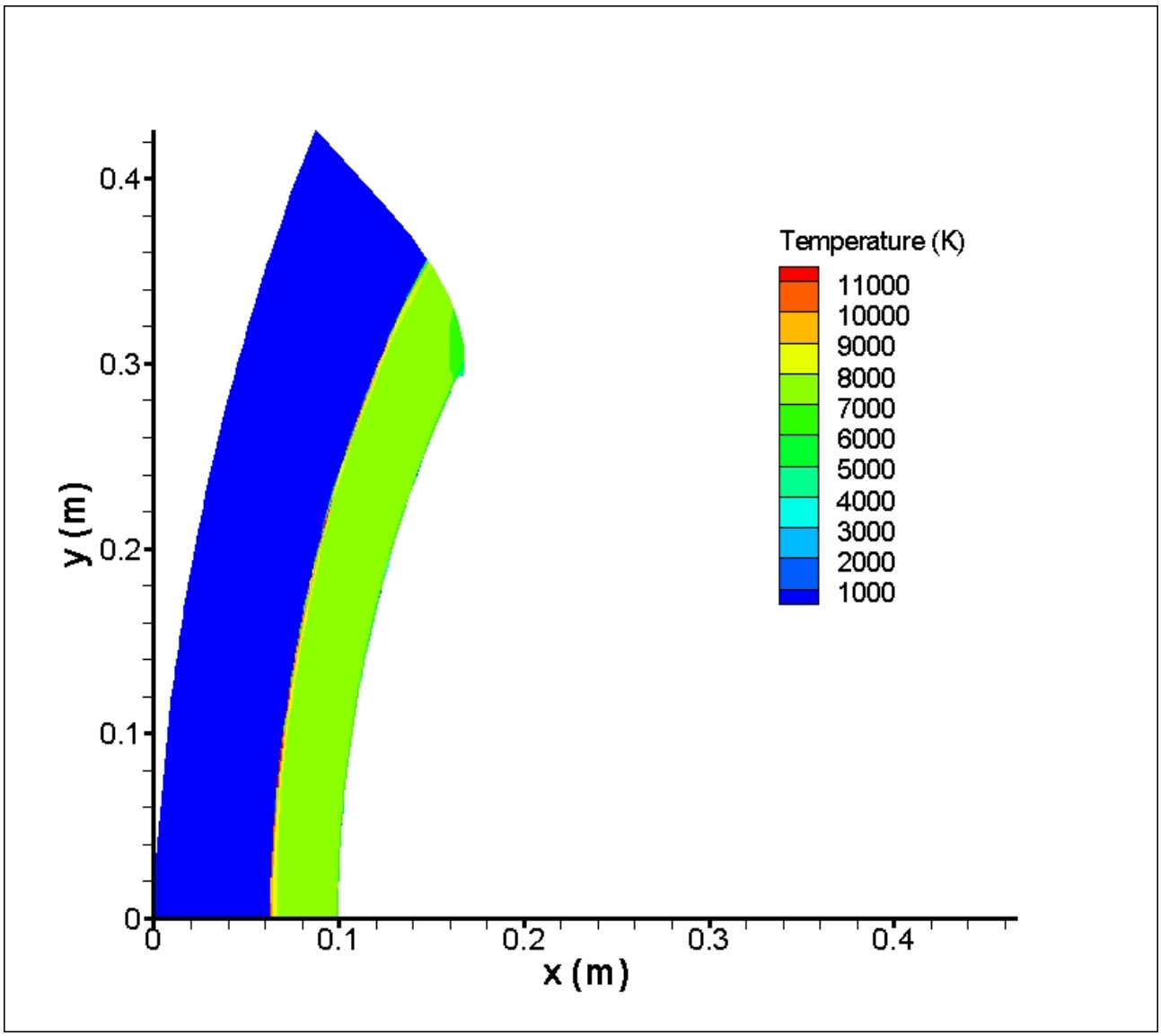
Temperature (K)
11000
10000
9000
8000
7000
6000
5000
4000
3000
2000
1000
y (m)
0
0.1
0.2
0.3
0.4
x (m)
0
0.1
0.2
0.3
0.4

Figure 2.

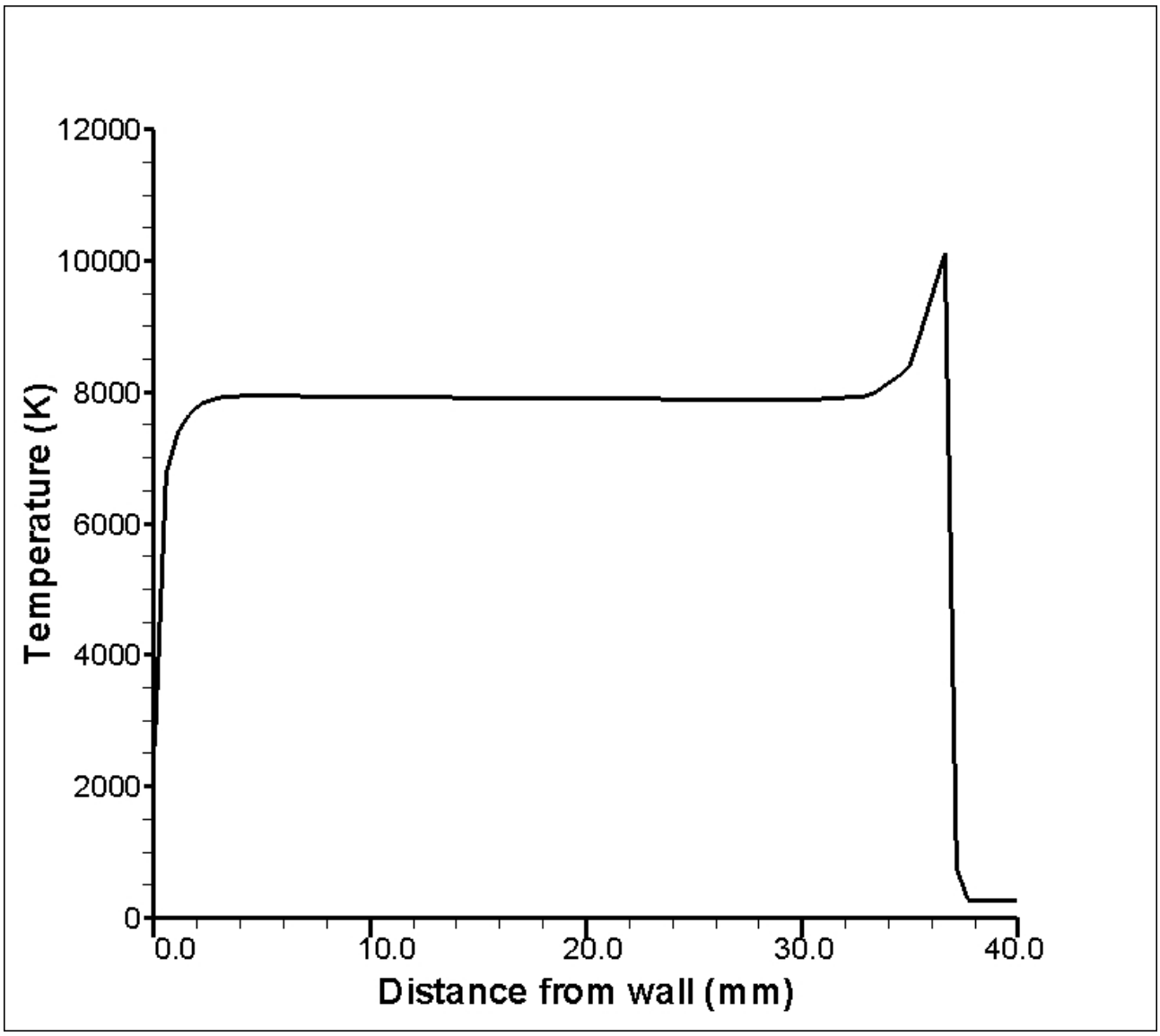
12000
10000
8000
6000
4000
2000
0
Temperature (K)
0.0
10.0
20.0
30.0
40.0
Distance from wall (mm)

Figure 3.

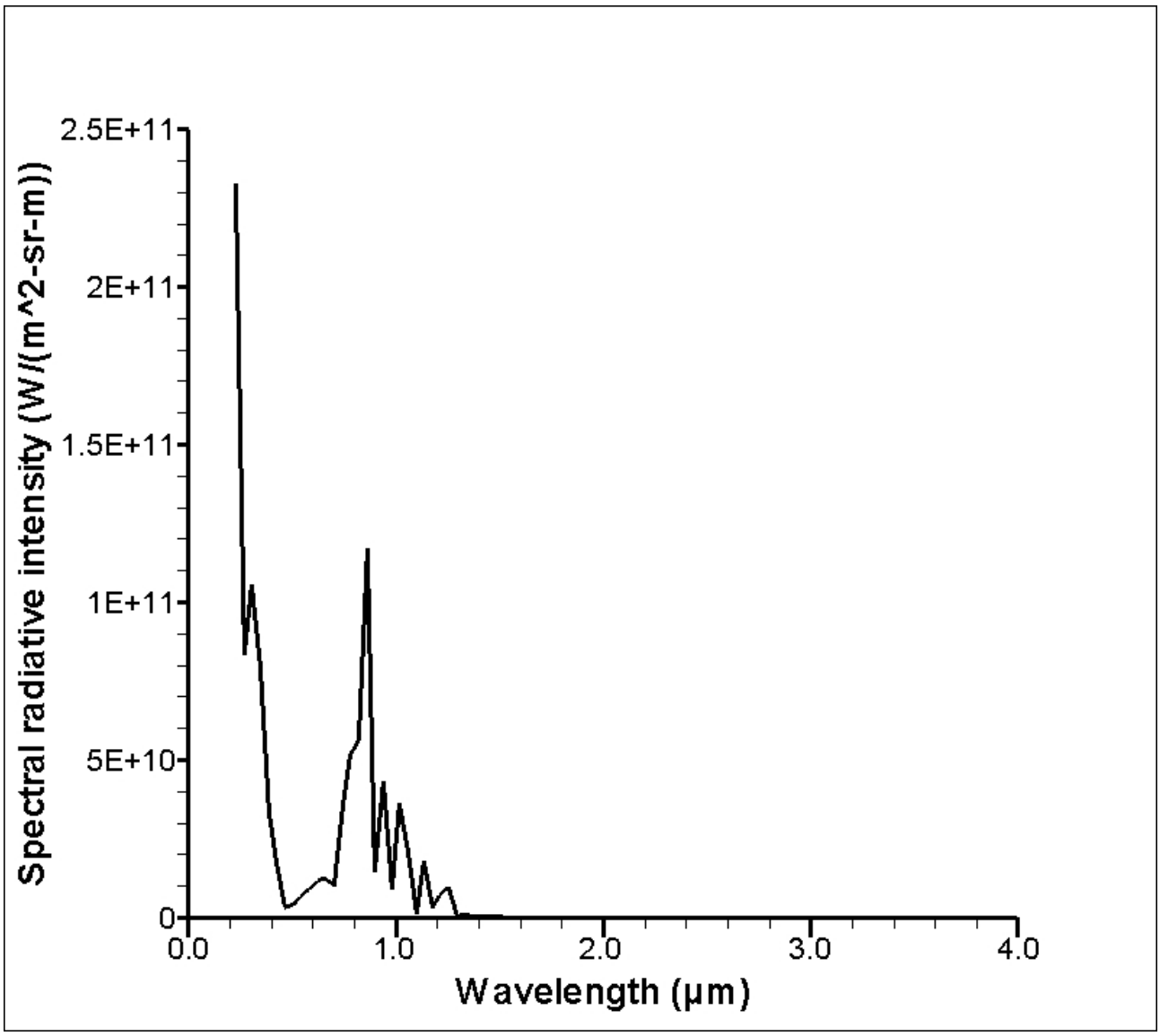
Spectral radiative intensity (W/(m^2-sr-m))
2.5E+11
2E+11
1.5E+11
1E+11
5E+10
0
0.0
1.0
2.0
3.0
4.0
Wavelength (µm)

Figure 4.

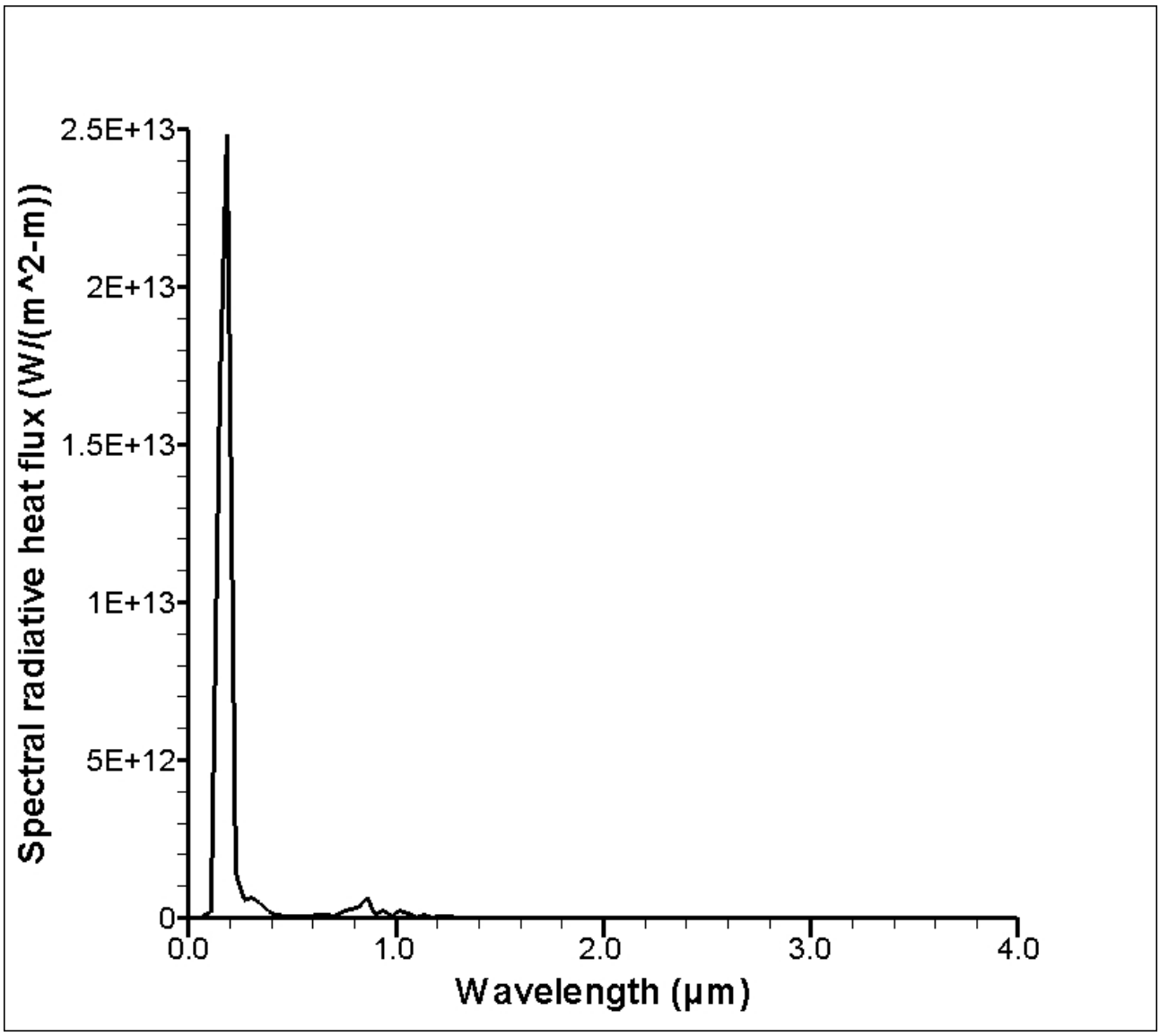
Spectral radiative heat flux (W/(m^2-m))
2.5E+13
2E+13
1.5E+13
1E+13
5E+12
0
0.0
1.0
2.0
3.0
4.0
Wavelength (µm)

Figure 5.

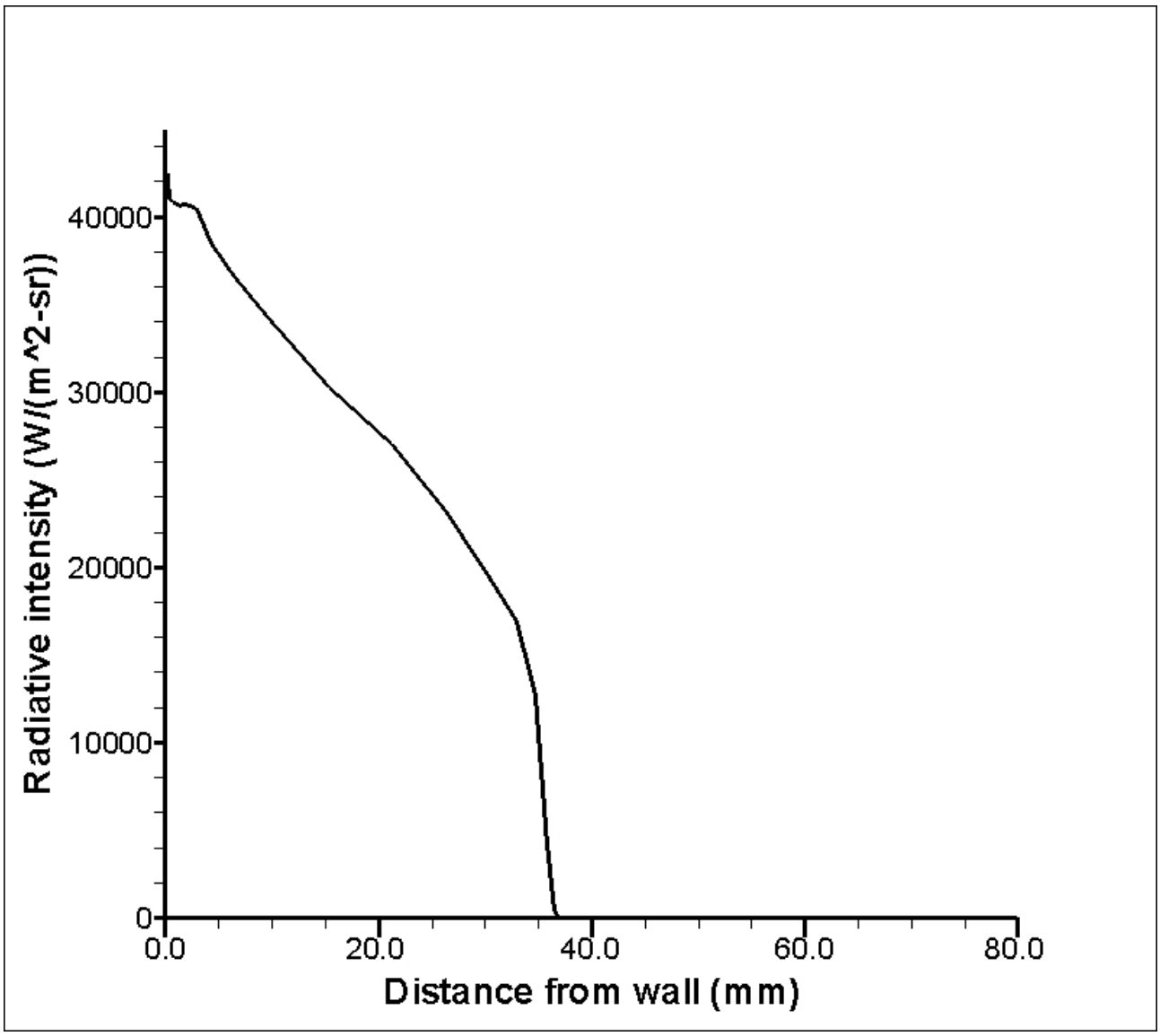
Radiative intensity (W/(m^2-sr))
40000
30000
20000
10000
0
0.0
20.0
40.0
60.0
80.0
Distance from wall (mm)

Figure 6.

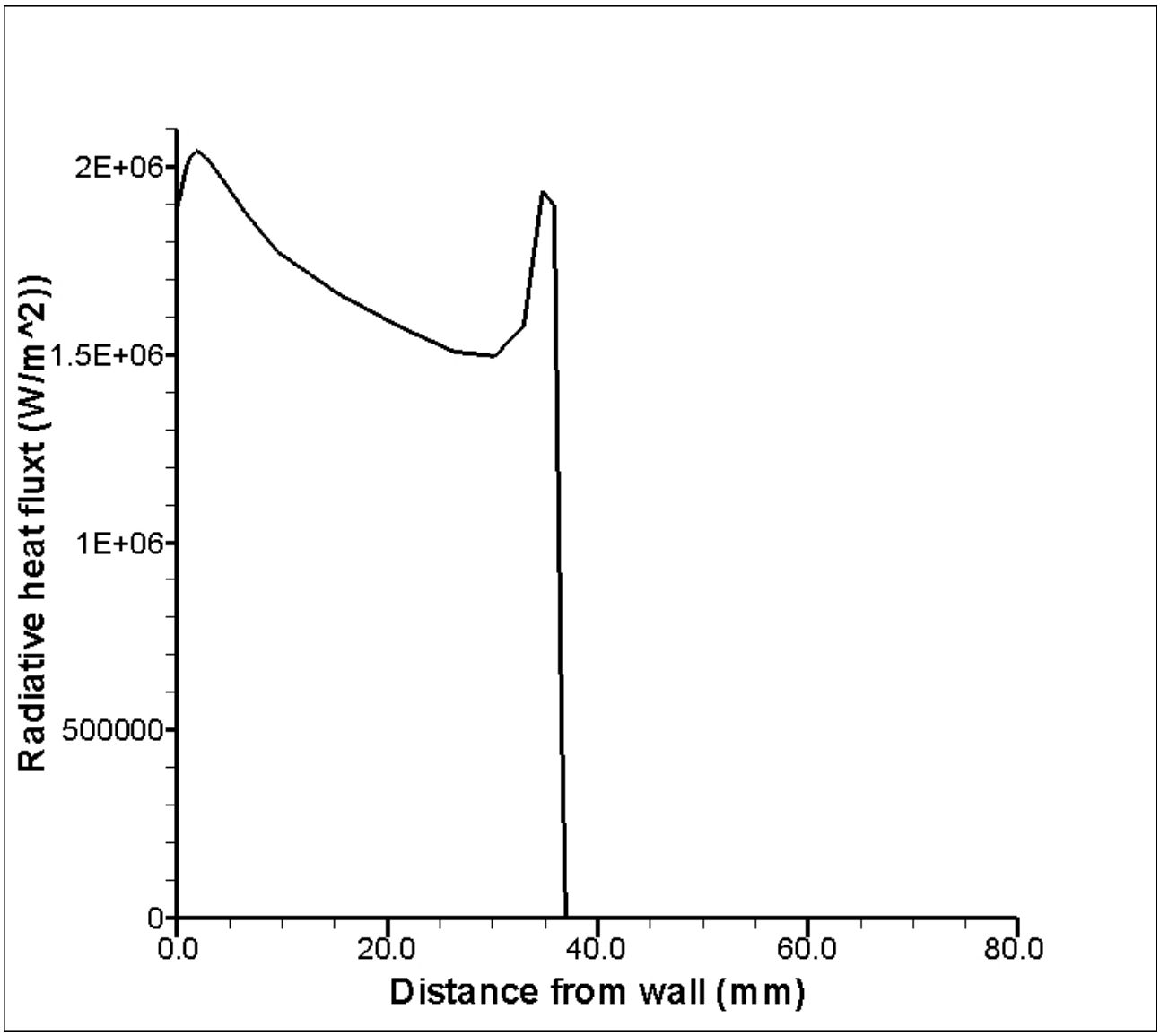
Radiative heat fluxt (W/m^2))
2E+06
1.5E+06
1E+06
500000
0
0.0
20.0
40.0
60.0
80.0
Distance from wall (mm)

Figure 7.

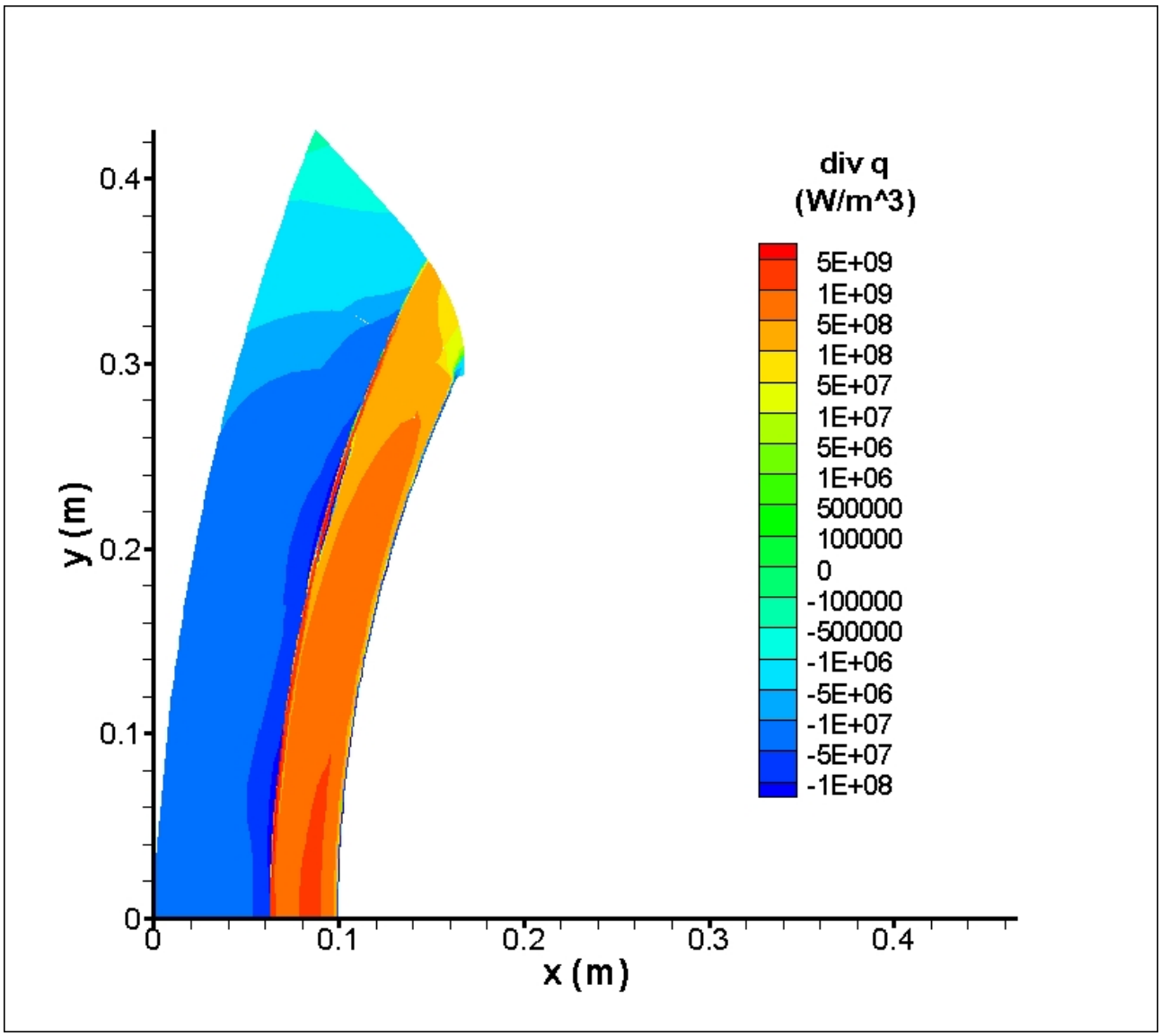
div q
(W/m^3)
5E+09
1E+09
5E+08
1E+08
5E+07
1E+07
5E+06
1E+06
500000
100000
0
-100000
-500000
-1E+06
-5E+06
-1E+07
-5E+07
-1E+08
y (m)
0
0.1
0.2
0.3
0.4
x (m)
0
0.1
0.2
0.3
0.4

Figure 8.

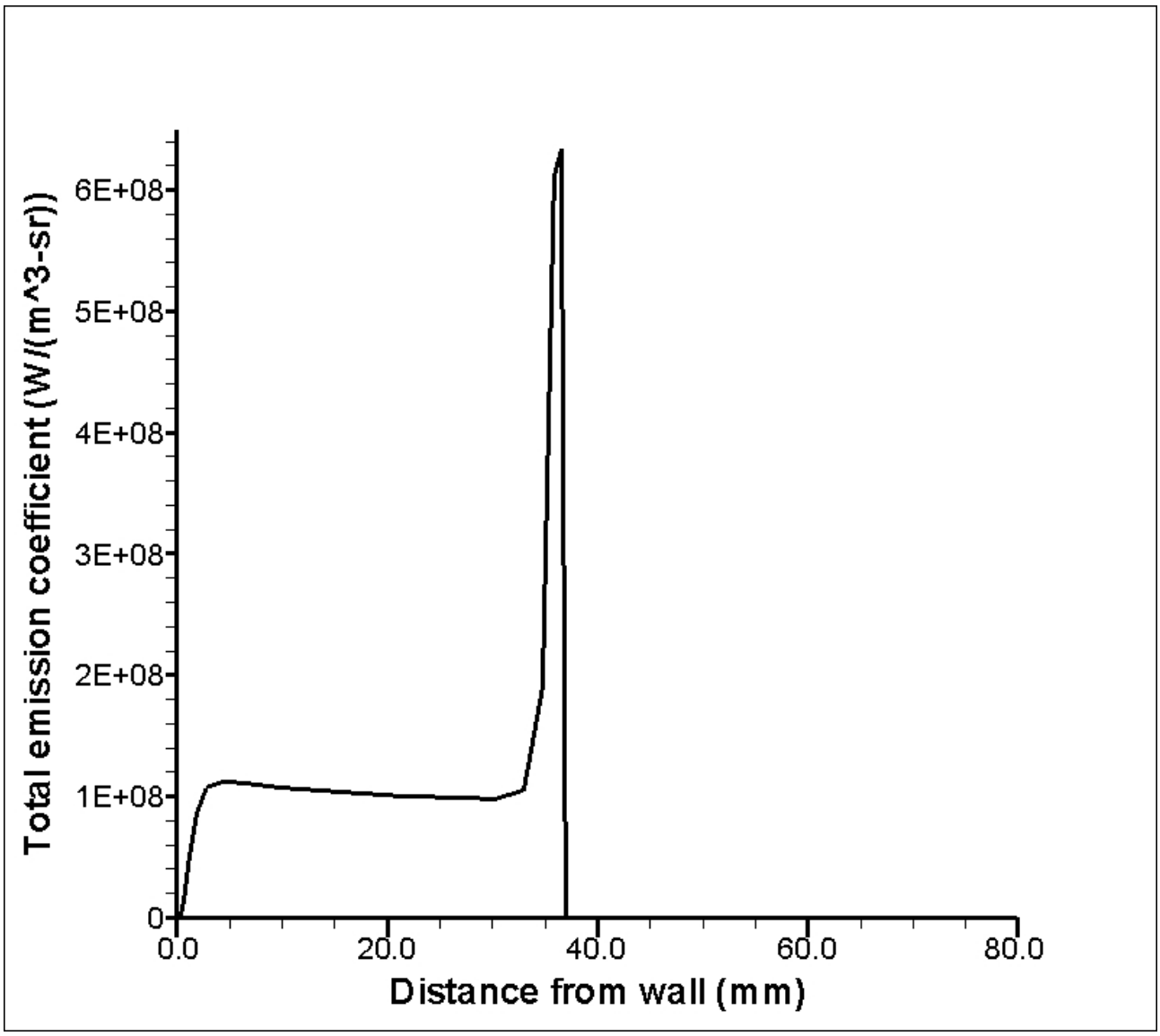
Total emission coefficient (W/(m^3-sr))
6E+08
5E+08
4E+08
3E+08
2E+08
1E+08
0
0.0
20.0
40.0
60.0
80.0
Distance from wall (mm)

Figure 9.

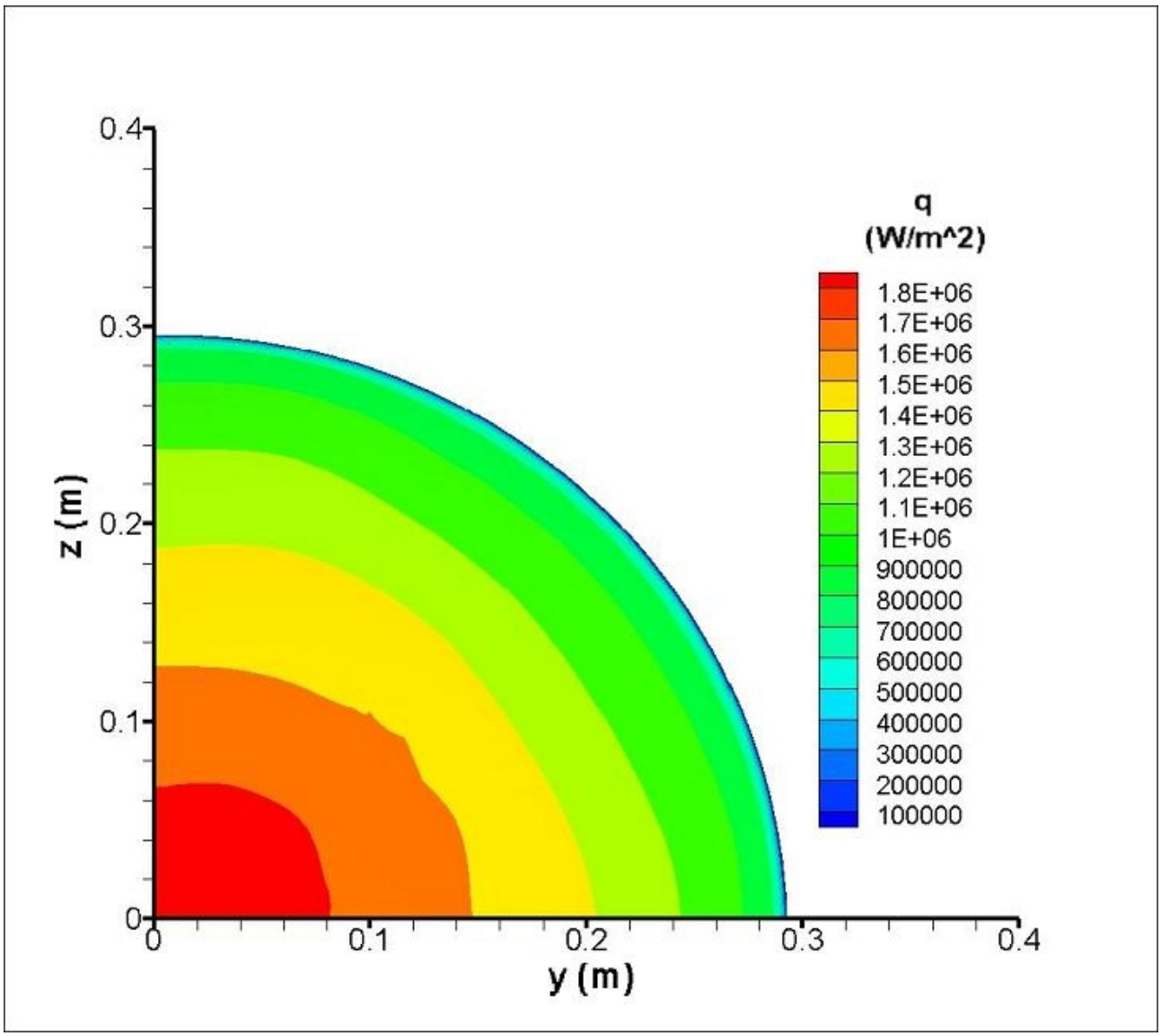
q
(W/m^2)
1.8E+06
1.7E+06
1.6E+06
1.5E+06
1.4E+06
1.3E+06
1.2E+06
1.1E+06
1E+06
900000
800000
700000
600000
500000
400000
300000
200000
100000
z (m)
0.4
0.3
0.2
0.1
0
0
0.1
0.2
0.3
0.4
y (m)

Figure 10.

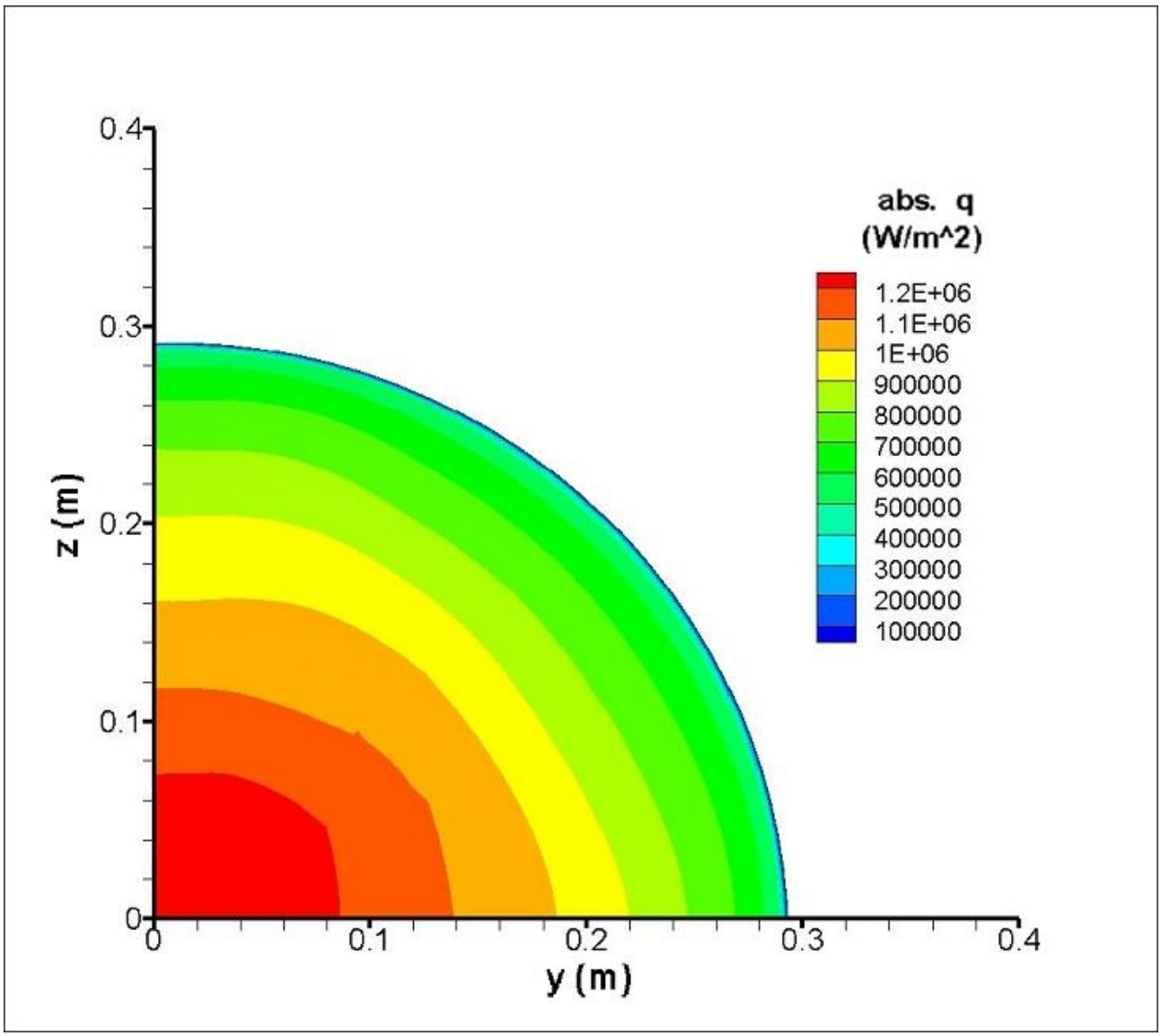
abs. q
(W/m^2)
1.2E+06
1.1E+06
1E+06
900000
800000
700000
600000
500000
400000
300000
200000
100000
z (m)
0.4
0.3
0.2
0.1
0
0
0.1
0.2
0.3
0.4
y (m)

Figure 11.